Supplementary Material for 'Sub-seasonal variability of supraglacial ice cliff melt rates and associated processes from time-lapse photogrammetry'

Table S1: Optimized accuracy of the different camera parameters for DEM processing with Agisoft Metashape.

Site	***Number of cameras***	***Optimized position accuracy (m)***		***Camera pose parameters accuracy (°)***		
		X, Y	***Z***	***Yaw***	***Pitch***	***Roll***
24K	4	0.1	0.5	5	5	5
Langtang	8	0.1	0.5	5	5	10

Table S2: Optimized accuracy of the PGCP position for DEM processing with Agisoft Metashape. The accuracy of the PGCPs is interpreted as a weighing coefficient describing the confidence we have in the PGCP position, therefore only the relative value between control points matters.

Site	***Number of PGCPs***	***Optimized X, Y, Z position accuracy range (m)***
24K	14	[0.1;0.5]
Langtang	21	[0.1;50]

Table S3: Characteristics of the DEM time-series for Langtang and 24K.

Site	***Number of cameras***	***Survey period***	***Number of DEMs***	***DEM resolution (m)***	***Maximum bias over background stable terrain (m)***
24K	4	08/06/2019-12/10/2019	19	0.24	0.05
Langtang	8	12/05/2019-01/11/2019	25	0.20	0.2

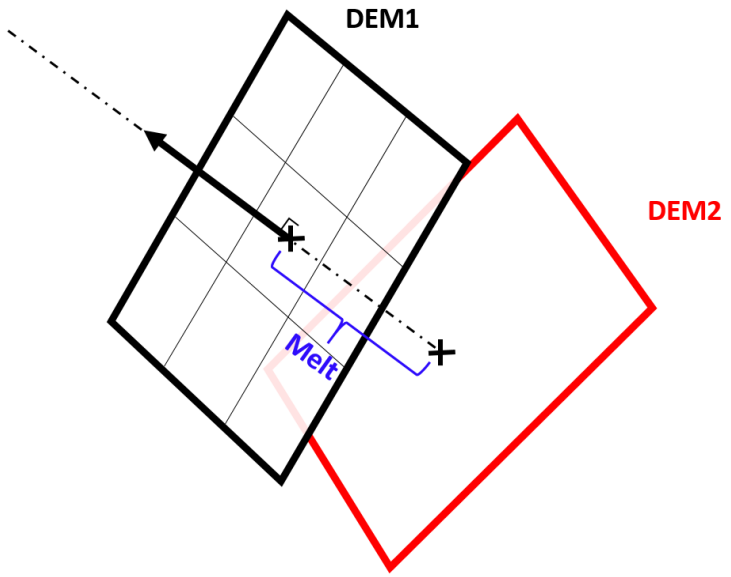

Figure S1: Melt calculation from two DEMs.

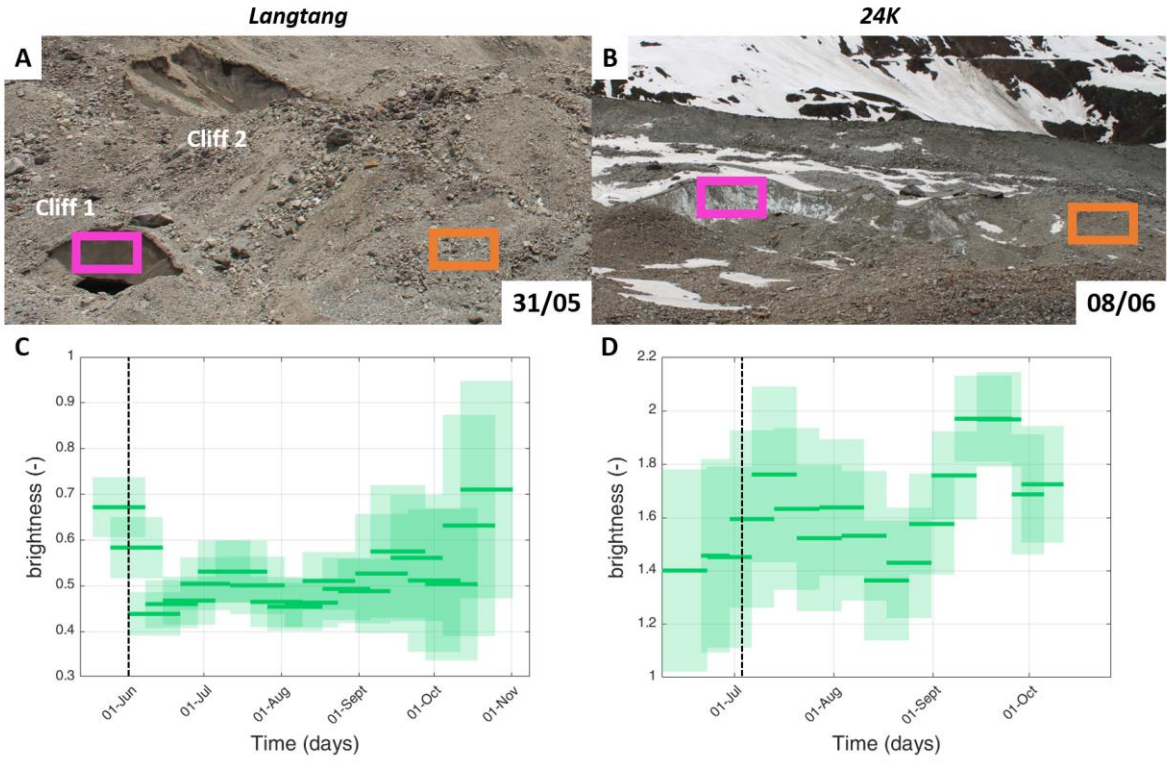

Figure S2: Brightness calculation for Langtang (A, C) and 24K (B, D). The boxes in the images represent the area over which the cliff brightness was calculated (pink) relative to the debris (orange). (C-D) Resulting brightness patterns averaged tri-weekly for Langtang and bi-weekly for 24K. The lines show the average brightness over the different periods and the shaded areas represent the standard deviation. Higher values at the beginning and the end

of the study period on Langtang coincide with a higher frequency of snow events. The vertical dashed lines show when the images were taken.

Table S4: Cliff melt for each surveyed cliff from the flow-corrected Pléiades (for Langtang), UAV (for 24K), as well as from the measured and modeled melt from the time-lapse time series. The UAV and Pléiades melt was calculated perpendicular to the slope of the initial DEM, as described in Section 5.4. Melt values were then integrated spatially (and temporally for the melt derived from the time-lapse), accounting for the cliffs' slope, to calculate the total volume losses. For the pre- and post-monsoon DEMs this spatial integration was conducted over 3 different domains: 1) the intersection of the cliff outlines in the pre and post-monsoon, 2) their union and 3) their union with a 4m buffer. The total volumes were then normalized by the domain area, and by the mean cliff planimetric area for the time-lapse values.

Melt (m w.e.day^{-1})	*Pre- and post-monsoon DEMs (Langtang: 2m Pléiades, 24K: 0.12m UAV)*			*Time-lapse DEMs*	
	Intersection	*Union*	*Union + 4m buffer*	*Measured*	*Modeled*
Langtang Cliff 1	0.020	0.017	0.017	0.039	0.041
Langtang Cliff 2	0.041	0.037	0.033	0.049	0.049
Langtang Cliff 3	0.045	0.034	0.032	0.047	0.046
24K Cliff	0.053	0.041	0.037	0.051	0.053

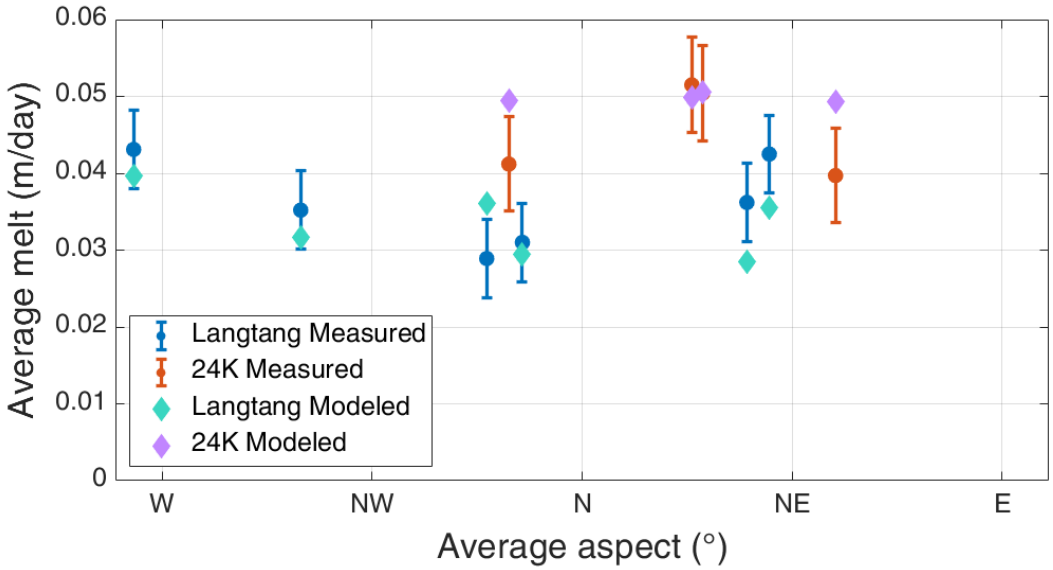

Figure S3: Average observed and modeled melt from the time-lapse camera data as a function of mean aspect from the time-lapse DEMs over the full study period for all the cliff focus areas. The bars indicate the uncertainty of the measured melt rates.

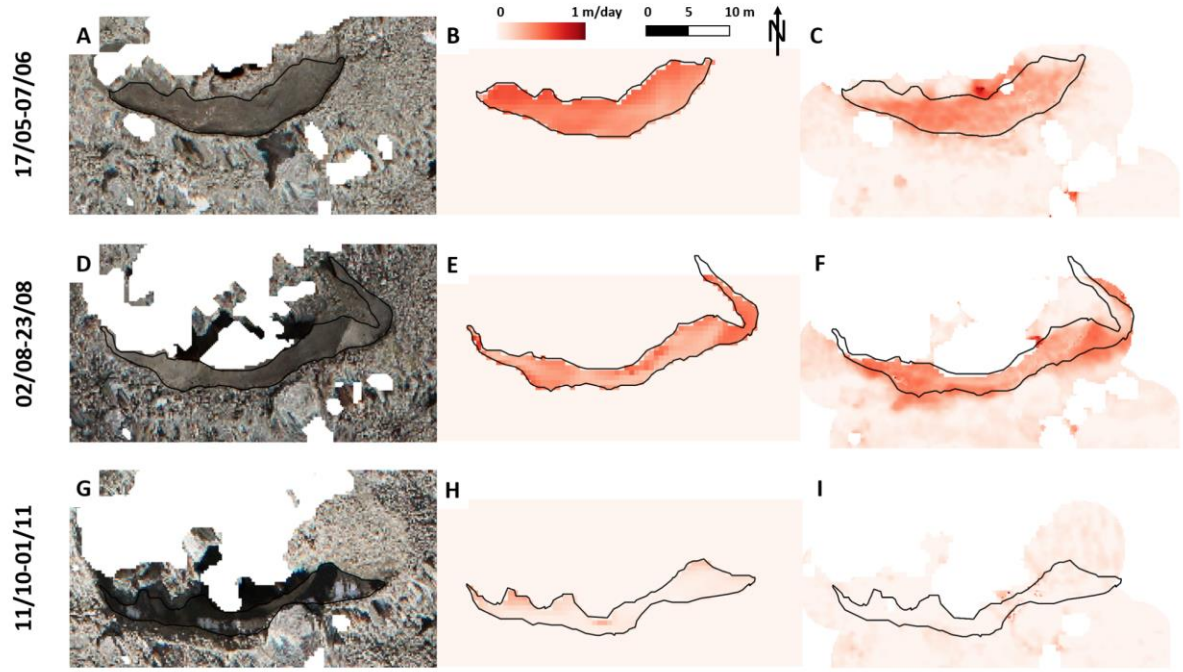

Figure S4: Orthoimages (left panels), modeled (central panels) and observed (right panels) melt patterns at the surface of Langtang cliff 1 (outlines in black) for the periods 17/05/2019 - 07/06/2019, 02/08/2019 - 23/08/2019 and 11/10/2019 - 01/11/2019.

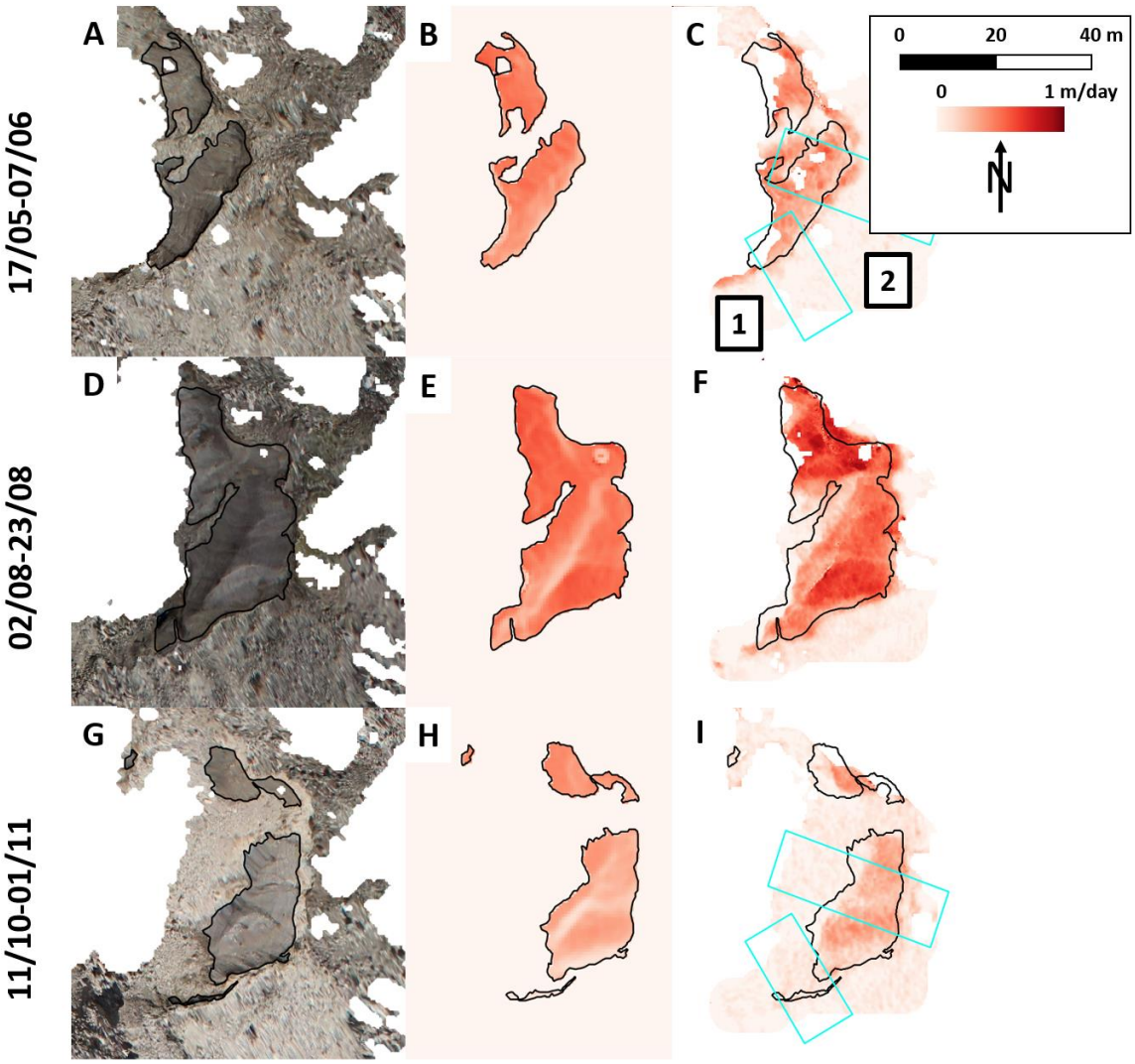

Figure S5: Orthoimages (left panels), modeled (central panels) and observed (right panels) melt patterns at the surface of Langtang cliff 2 (outlines in black) for the periods 17/05/2019 - 07/06/2019, 02/08/2019 - 23/08/2019 and 11/10/2019 - 01/11/2019.

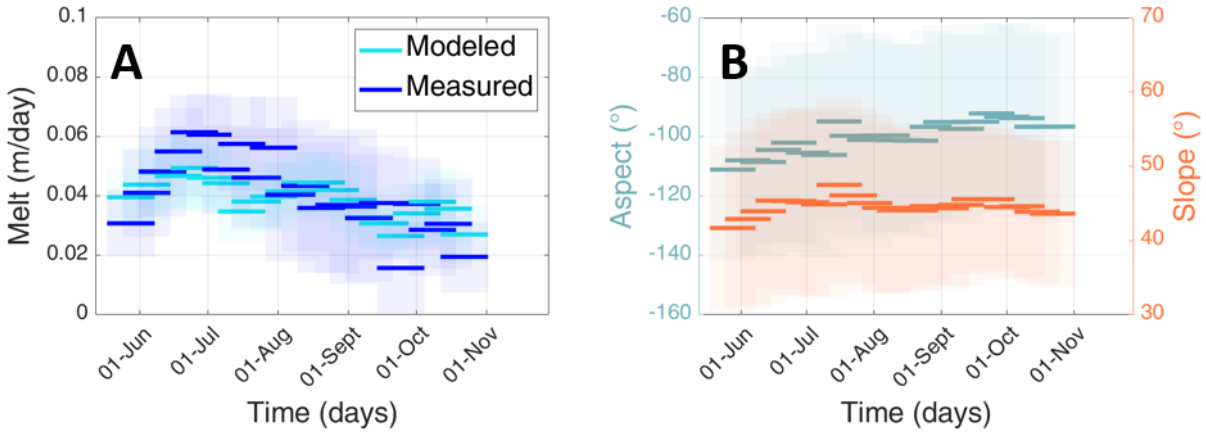

Figure S6: Measured and modeled melt (A) and aspect and slope (B) evolution of Langtang Cliff 2.

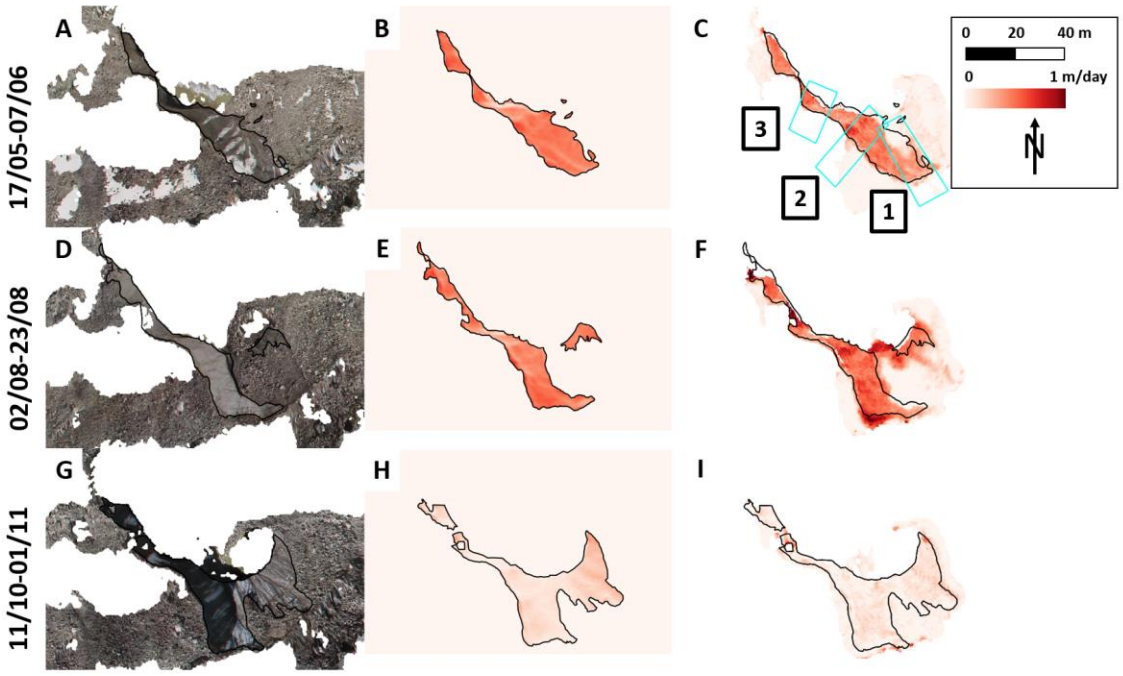

Figure S7: Orthoimages (left panels), modeled (central panels) and observed (right panels) melt patterns at the surface of Langtang cliff 3 (outlines in black) for the periods 17/05/2019 - 07/06/2019, 02/08/2019 - 23/08/2019 and 11/10/2019 - 01/11/2019.

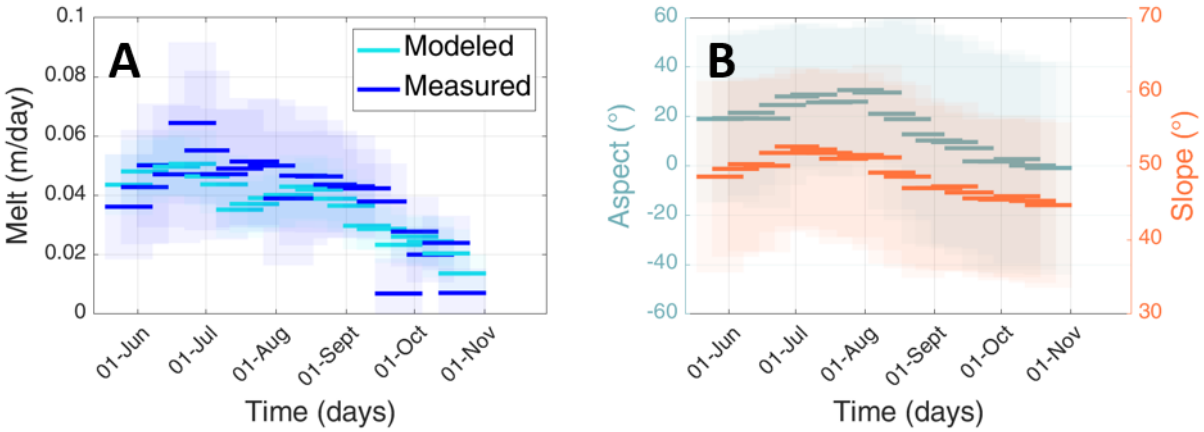

Figure S8: Measured and modeled melt (A) and aspect and slope (B) evolution of Langtang Cliff 3.

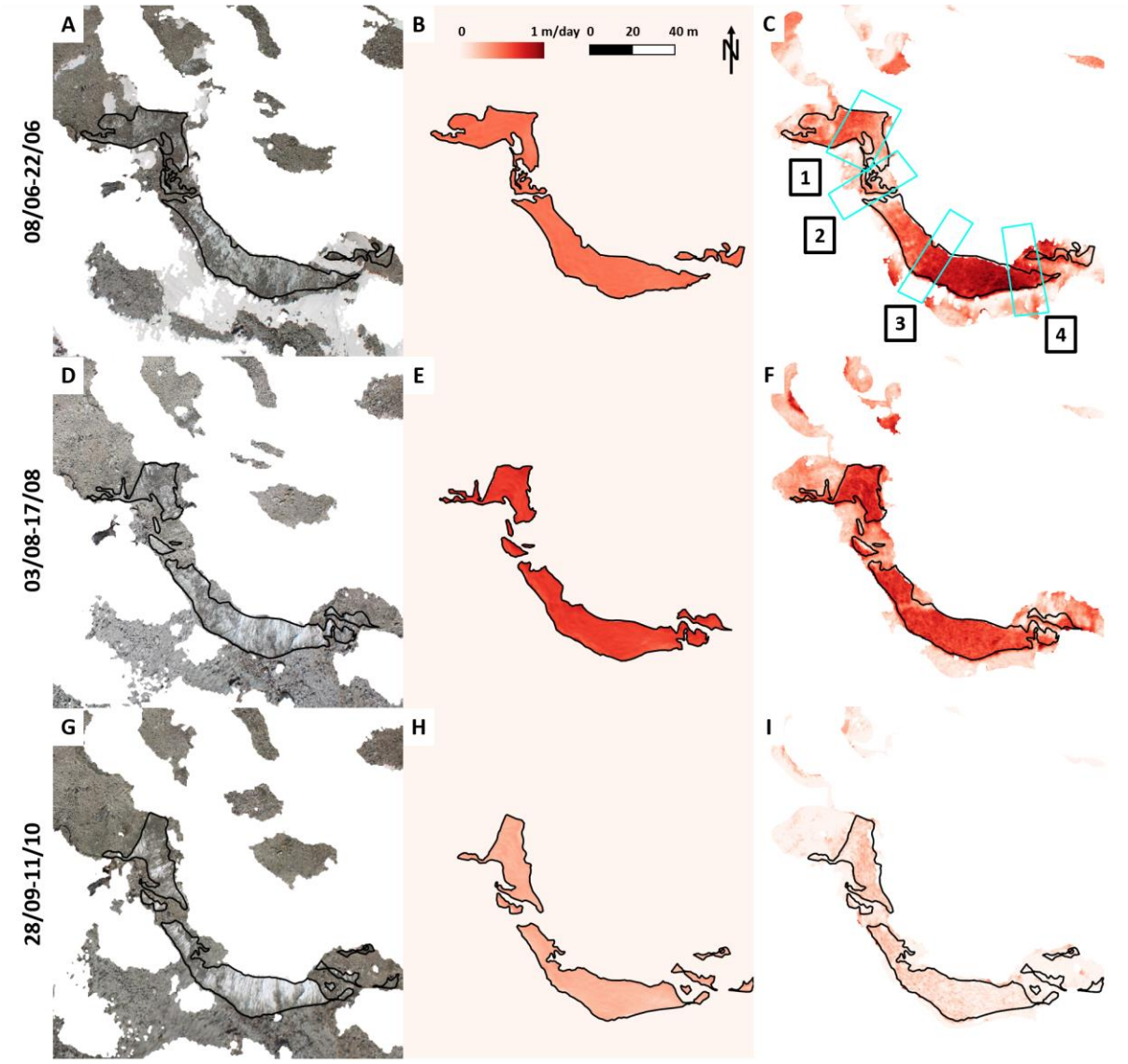

Figure S9: Orthoimages (left panels), modeled (central panels) and observed (right panels) melt patterns at the surface of the 24K cliff (outlines in black) for the periods 08/06/2019 - 22/06/2019, 03/08/2019 - 17/08/2019 and 28/09/2019 - 11/10/2019.

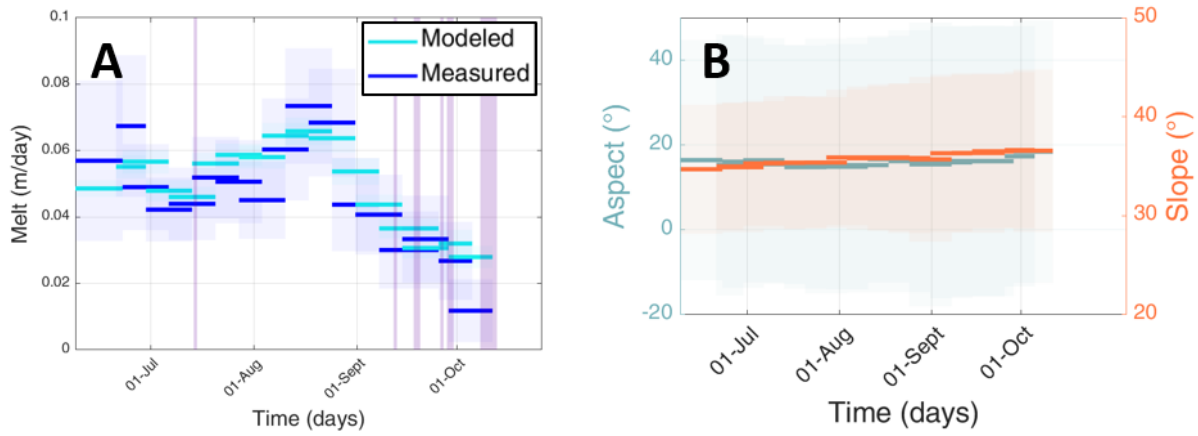

Figure S10: Measured and modeled melt (A) and aspect and slope (B) evolution of the 24K cliff.

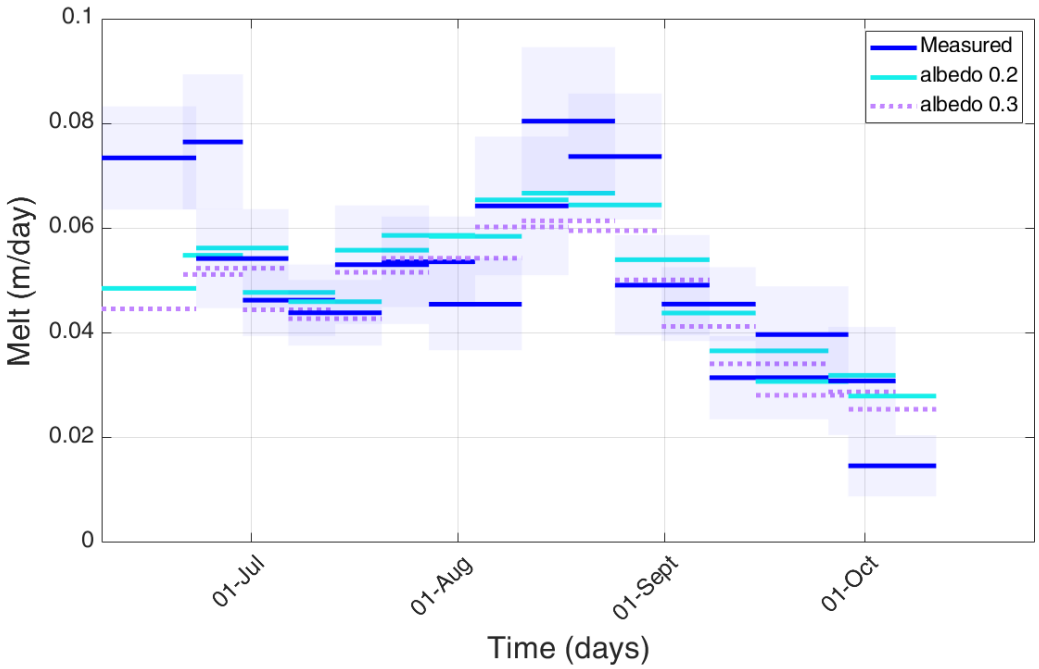

Figure S11: Observed (dark blue) and modeled melt rates of the 24K transect 3 during the whole study periods with fixed cliff albedo values of 0.2 (light blue full lines) and 0.3 (purple dashed lines). The dark blue patches show the standard deviation of the measured melt rates.

Section S1. Use of time-lapse photogrammetry approach

We assembled a custom-built weather-proof time-lapse setup, designed to run fully autonomously for several months while taking high-quality images. The setup was relatively expensive (~1900 € per camera), with the additional constraint of weight in the field, as each setup represented ~15 kg to carry to installation location. These logistical aspects, in addition to the structure-from-motion considerations (Mallalieu et al., 2017), constrained the choice of the survey areas considerably. The setup was relatively easy and quick to install in the field once all elements had been brought to the installation site, each camera requiring 2-3 hours to be deployed. The cameras all ran without interruption during the whole study period, and even longer for the 24K cameras. These were indeed left to run as 'fixed' stations and were still in excellent condition when last checked in summer 2021, two years after their initial installation, despite some observation gaps in the winter due to power shortages caused by limited direct sun illumination and snow accumulation on the solar panels.

The processing of the image sets was fully automated except for the identification of the PGCPs, and followed the general workflow proposed by Mallalieu et al. (2017) in Agisoft Metashape. Once all the scripts were running in an automated way, the processing of an image set to the DEM and orthoimage took between 1 and 1.5 hours, with the main constraint being the manual positioning of the PGCPs (Mallalieu et al., 2017). As was to be expected, the measurement errors depended on the distance from the cameras, time since the reference image set (Fig. 5), and to some extent the illumination and atmospheric

conditions (Mallalieu et al., 2017; Smith and Vericat, 2015). Indeed, images with strong direct illumination or those which were blurred by local rain events or low clouds usually resulted in high biases relative to the reference image sets. However, the higher number of cameras on Langtang did not seem to reduce this error, possibly because the viewing angles were too similar (Bemis et al., 2014). While the spread in the elevation data had a limited influence on our results, we found that the systematic error, which we estimated to be +/- 20 cm (+/- 6 cm) at the cliff site for Langtang (24K), was the main constraint to study the cliff changes at high temporal frequency. These 1:1500 to 1:5000 errors are in the low range of previous time-lapse photogrammetry surveys, which were between 1:650 (Smith and Vericat, 2015), 1:1000 (James and Robson, 2012; Mallalieu et al., 2017) and 1:3500 (Filhol et al., 2019), which is likely at least partly related to the quality of the sensors.

The high-quality DEMs and elevation change measurements resulting from the time-lapse survey confirm the robustness of such a setup to monitor surface changes relative to other more expensive devices such as TLS (Bemis et al., 2014; Piermattei et al., 2015).

References

Bemis, S. P., Micklethwaite, S., Turner, D., James, M. R., Akciz, S., Thiele, S. T., and Bangash, H. A.: Ground-based and UAV-Based photogrammetry: A multi-scale, high-resolution mapping tool for structural geology and paleoseismology, J. Struct. Geol., 69, 163–178, https://doi.org/10.1016/j.jsg.2014.10.007, 2014.

Filhol, S., Perret, A., Girod, L., Sutter, G., Schuler, T. V., and Burkhart, J. F.: Time- Lapse Photogrammetry of Distributed Snow Depth During Snowmelt, Water Resour. Res., 55, 7916–7926, https://doi.org/10.1029/2018WR024530, 2019.

James, M. R. and Robson, S.: Straightforward reconstruction of 3D surfaces and topography with a camera: Accuracy and geoscience application, J. Geophys. Res. Earth Surf., 117, n/a-n/a, https://doi.org/10.1029/2011JF002289, 2012.

Mallalieu, J., Carrivick, J. L., Quincey, D. J., Smith, M. W., and James, W. H. M.: An integrated Structure-from-Motion and time-lapse technique for quantifying ice-margin dynamics, J. Glaciol., https://doi.org/10.1017/jog.2017.48, 2017.

Piermattei, L., Carturan, L., and Guarnieri, A.: Use of terrestrial photogrammetry based on structure-from-motion for mass balance estimation of a small glacier in the Italian alps, Earth Surf. Process. Landforms, 40, 1791–1802, https://doi.org/10.1002/ESP.3756, 2015.

Smith, M. W. and Vericat, D.: From experimental plots to experimental landscapes: topography, erosion and deposition in sub- humid badlands from Structure- from- Motion photogrammetry, Earth Surf. Process. Landforms, 40, 1656–1671, https://doi.org/10.1002/esp.3747, 2015.